RSC Advances

PAPER

View Article Online
View Journal | View Issue

Cite this: *RSC Adv.*, 2019, **9**, 19930

Structure and photocatalytic performance of rice husk-like Ba-doped GaOOH under light irradiation

Panqi Huang and Jingfei Luan*

The effects of Ba-doping on the structure and photocatalytic performance of GaOOH were investigated for the first time in this paper. XRD, SEM, TEM, XPS, UPS, FT-IR, UV-Vis DRS, PL, BET and EPR characterizations were carried out to analyze the properties of Ba-doped GaOOH. The results showed that GaOOH crystallized well with the orthorhombic crystal system with space group *Pbnm*. The lattice parameters of GaOOH were found to be $a = 4.509526$ Å, $b = 9.771034$ Å and $c = 2.969284$ Å. The transition in the structural morphology of GaOOH before and after Ba-doping was observed in SEM pictures in which the morphology of GaOOH varied from wood-like to rice husk-like. At the same time, the specific surface area of 4 wt% Ba-doped GaOOH (21.5854 $m^2 g^{-1}$) was 3.42 times that of pure GaOOH (6.3047 $m^2 g^{-1}$). Ba-doping caused a red shift of the band gap according to UV-Vis DRS results. The enhanced defect states caused by Ba-doping was confirmed by PL results, which decreased the recombination rate of photogenerated electrons and photogenerated holes. Compared with pure GaOOH, when GaOOH with different Ba content was used as photocatalyst, the removal rate of enrofloxacin was increased by more than 20% only by illumination for 60 min. In addition, Ba-doped GaOOH had excellent stability and could be reused, which could reduce costs and increase the potential of its practical application.

Received 15th May 2019
Accepted 17th June 2019

DOI: 10.1039/c9ra03670a

rsc.li/rsc-advances

Introduction

GaOOH (gallium oxyhydroxide), a wide band gap (4.75 eV) semiconductor material, has been extensively prepared and is often used as a photocatalyst and as a precursor for the preparation of various gallium-containing compounds, such as Ga_2O_3, GaN and $ZnGa_2O_4$.[1–10] Many ways have been found to prepare GaOOH with different morphologies and properties.[11–15] A hydrothermal method with ionic liquid aide was found to prepare α-GaOOH with layered structure by D. Li *et al.*[16] Wedge-like α-GaOOH particles were prepared by F. Shiba *et al.*[17] through the hydrolysis process, using sodium acetate as a growth regulator. Electrochemical oxidation of gallium based liquid metals was used to prepare GaOOH in the study of B. Lertanantawong *et al.*[18] Using oxalic acid to form various forms of α-GaOOH at different temperatures during hydrothermal processes was studied by M. Muruganandham *et al.*[19] Y. H. Hsu *et al.* prepared Au-modified GaOOH nanorods to improve performance of methanol fuel cells under light irradiation.[20]

Metal ion doping technology has been regarded as one of the effective ways to construct surface defects of semiconductor materials and improve the surface characteristics.[21–26] According to the A. Firdous's report,[27] after Ba doping, the absorption edge of ZnS moved towards the blue region and the optical band gap of ZnS reduced, enhancing potential applications for ZnS. It was also observed in G. Srinet's report[28] that band gap redshifted and defect states was enhanced for ZnO after Ba-doping. Meanwhile, before and after Ba-doping, the nanostructure morphology of ZnO changed. There were few reports on metal ion doping of GaOOH, mainly focusing on the lanthanide metal ion, such as Dy(3+),[29] Eu(3+)[30,31] and Ln(3+),[32–36] and both are applied as fluorescent materials and precursors. The doping of GaOOH with a main group metal ion and its direct use as a photocatalyst have not been reported. Therefore, this paper reports the Ba-doped GaOOH for the first time. In this paper, XRD (X-ray diffraction), SEM (scanning electron microscopy), TEM (transmission electron microscopy), XPS (X-ray photoelectron spectroscopy), UPS (ultraviolet photoelectron spectroscopy), FT-IR (Fourier transform infrared spectroscopy), UV-Vis DRS (UV-Vis diffuse reflectance spectroscopy), BET (Brunauer–Emmett–Teller method), PL (fluorescence spectroscopy) and EPR (electron paramagnetic resonance spectroscopy) were utilized to analyze the structural properties of pure GaOOH and Ba-doped GaOOH prepared by us. In addition, the removal rate of enrofloxacin under illumination with pure GaOOH or Ba-doped GaOOH as a photocatalyst was measured.

Experimental

Preparation of pure GaOOH and Ba-doped GaOOH

In this paper, solvothermal method was selected to prepare pure GaOOH and Ba-doped GaOOH. Specific steps to prepare

State Key Laboratory of Pollution Control and Resource Reuse, School of the Environment, Nanjing University, Nanjing 210093, China. E-mail: jfluan@nju.edu.cn

Ba-doped GaOOH were as follows: (I) 1.1296 g Ga_2O_3 (purity of 99.99%, Aladdin Biochemical Technology Co., Ltd., Shanghai, China) was accurately weighed and placed in a 250 mL beaker and then 80 mL of deionized water and 80 mL of absolute ethanol were added. (II) According to the requirement of different doping amount, Ba $(NO_3)_2$ (purity of 99.9%, Sinopharm Group Chemical Reagent Co., Ltd., Shanghai, China) was added accurately to above beaker. The doping amount (the mass ratio of Ba element to GaOOH) was set to 4%, 8%, 16%, respectively. (III) 1 mol L^{-1} sodium hydroxide solution was added dropwise to adjust the pH to 13. (IV) After stirring at room temperature for 30 min, the above solution was transferred from the beaker to a 200 mL tetrafluoro-lined reactor and heated at 200 °C for 12 h. (V) After the completion of the heating, it was cooled to room temperature, washed several times with water and absolute ethanol, and then dried at 60 °C for 12 h, and finally grinded into powders. The resulting products were marked as 4 wt% Ba-doped GaOOH, 8 wt% Ba-doped GaOOH and 16 wt% Ba-doped GaOOH, respectively. Pure GaOOH was prepared as a control sample according to the above steps with no Ba $(NO_3)_2$ added.

Characterization of pure GaOOH and Ba-doped GaOOH

Some scientific methods were selected to analyze pure GaOOH and Ba-doped GaOOH catalysts prepared above. Powder X-ray diffractometer (XRD, D/MAX-RB, Rigaku Corporation, Japan) was selected to analyze the crystal form of pure GaOOH and Ba-doped GaOOH. The instrument adopted CuKα radiation (λ = 1.54056) and collected data using step-scan program at 295 K. Scan range was set to 15–45°. Time per step and step interval was 1.2 second and 0.04°. Scanning electron microscope (SEM, LEO 1530VP, LEO Corporation, Dresden, Germany) was selected to analyze the morphological features of pure GaOOH and Ba-doped GaOOH. Transmission electron microscopy (TEM, Tecnai F20 S-Twin, FEI Corporation, Hillsboro, OR, USA) was selected to analyze the morphology and selected diffraction spot of pure GaOOH and Ba-doped GaOOH. X-ray photoelectron spectroscopy (XPS, ESCALABMK-2, VG Scientific Ltd., London, UK) was selected to analyze the Ga^{3+} content, Ba^{2+} content and O^{2-} content of Ba-doped GaOOH. Fourier transform infrared spectrometer (Nexus, Nicolet Corporation, Madison, WI, USA) with an attenuated total reflectance (ATR) mode was selected to analyze the main chemical vibrational species of pure GaOOH and Ba-doped GaOOH. Full-function fluorescence spectrometer (Fluoromax-4, Horiba Scientific) was selected to analyze the photoluminescence properties of pure GaOOH and Ba-doped GaOOH. UV-Vis spectrophotometer (UV-2450, Shimadzu Corporation, Kyoto, Japan) was selected to measure UV-visible diffuse reflectance spectra of pure GaOOH and Ba-doped GaOOH catalysts and blank background material was $BaSO_4$. Brunauer–Emmett–Teller (BET) method (ASAP 2020 V3.00 H, USA) with N_2 adsorption at liquid nitrogen temperature was selected to measure the specific surface areas of pure GaOOH and Ba-doped GaOOH. Electron paramagnetic resonance spectrometer (EPR, EMX-10/12, Bruker, German) was selected to analyze hydroxyl radical ($\cdot$OH) and superoxide radical ($\cdot O_2^-$).

Photocatalytic performance of pure GaOOH and Ba-doped GaOOH

The photocatalytic performance of pure GaOOH and Ba-doped GaOOH catalysts was analyzed by degrading enrofloxacin, an antibiotic that was difficult to biodegrade and its accumulation was very harmful to the human body. A photocatalytic reactor (Xujiang Machine, Nanjing, China) was selected to carry out photocatalytic reactions. The photocatalytic reactor included a mercury lamp (500 W), optical filters and a magnetic stirring device. The major emission wavelength of the mercury lamp we used in this paper was 365 nm and the spectral distribution and relative energy of the mercury lamp was shown in Table 1. In addition, the optical filters could filter out light with a wavelength greater than 400 nm, which meant that only ultraviolet light with a wavelength of less than 400 nm could pass through the optical filters to irradiate the reaction tubes containing the contaminant solution and the catalyst sample. The parameters of photocatalytic experiment were as follows: the initial concentration of enrofloxacin was set to be 10 mg L^{-1}, the catalyst dosage was set to be 1 g L^{-1} and the time of ultraviolet light irradiation was set to be 120 min. In the experiment process, 0.05 g catalyst was weighed and added to a test tube containing 50 mL of enrofloxacin solution. The above tube was placed in the photocatalytic reactor and magnetically stirred for half an hour under dark conditions for dark adsorption. Then ultraviolet light irradiation was carried out. 2 mL of the solution was taken under ultraviolet light for 10 min, 20 min, 30 min, 40 min, and 60 min, and the absorbance of enrofloxacin was measured at 276 nm using the UV-visible spectrophotometer (UV-2550, Shimadzu Corporation, Kyoto, Japan).

The absorbency standard curve of enrofloxacin was obtained by measuring the absorbance of enrofloxacin at a concentration of 2 mg L^{-1}, 4 mg L^{-1}, 6 mg L^{-1}, 8 mg L^{-1}, 10 mg L^{-1} and 12 mg L^{-1}, respectively. Then the linear relationship between the concentration of enrofloxacin and the absorbance was obtained by linear simulation. The removal rate of enrofloxacin (D%) was calculated by the following equation: $D\% = (C_0 - C_t)/C_0 \times 100\%$, where C_0 was the initial concentration of enrofloxacin and C_t was the concentration of enrofloxacin at time t.

Results and discussion

Characterization

XRD analysis. Fig. 1 shows the powder X-ray diffraction patterns and Pawley refinements of GaOOH with different Ba-doping amount and pure GaOOH. We used the Materials Studio program to refine the XRD raw data of all samples using the Pawley analysis method. When the R factor was less than 20%, it meant that the XRD experimental test data of the sample was in good agreement with the theoretical data.[37] In this paper, the R factor of pure GaOOH prepared by us was only 9.85%, revealing that the pure GaOOH was prepared successfully with a orthorhombic crystal system and a space group *Pbnm*, and the lattice parameters of pure GaOOH were a = 4.509526 Å, b = 9.771034 Å and c = 2.969284 Å, which was almost consistent with the reported results (orthorhombic, *Pbnm*, a = 4.5545 Å, b = 9.8007 Å and c = 2.9738 Å).[38] The first five peaks at 2θ =

Table 1 Spectral distribution and relative energy of a mercury lamp

Wavelength (nm)	265.2–265.5	296.7	302.2–302.8	312.6–313.2	365.0–366.3	404.5–407.8	435.8	546.1	577.0–579.0
Relative energy (%)	15.3	16.6	23.9	49.9	100.0	42.2	77.5	93.0	76.5

21.76°, 34.00°, 35.41°, 37.46° and 54.54° were all observed clearly for pure GaOOH and Ba-doped GaOOH in Fig. 1, corresponding to the (110), (130), (021), (111) and (221) crystal planes, respectively. In addition, *R* factors of 4 wt%, 8 wt% and 16 wt% Ba-doped GaOOH were 10.47%, 18.28% and 14.05%, respectively, which were less than 20%, indicating that the XRD diffraction pattern of Ba-doped GaOOH was consistent with the theoretical XRD pattern of pure GaOOH. In other words, it could be considered that the Ba doping did not substantially change the basic crystal structure of GaOOH.

SEM, TEM and BET analysis. Fig. 2 shows the scanning electron microscope pictures of GaOOH with different Ba-doping amount and the pure GaOOH under the same magnification conditions. As we could see from Fig. 2, the morphology of GaOOH was quite different before and after Ba-doping. After the Ba-doping, the morphology of GaOOH changed dramatically, which transformed from wood-like structure to rice husk-like structure. The change in morphology was attributed to Ba ions on the surface.[28] In the nucleation process, surface Ba ions accelerate the growth of particles by interparticle attraction.[39] As we could see from Fig. 2(b–d), lots of fibrous independent structures were at both ends of Ba-doped GaOOH. In addition, it could be discovered that when the amount of Ba-doping increased to 8 wt% and 16 wt%, some fibrous structures at both ends of the prepared catalyst were broken. The grinding operation during catalyst preparation might be one of the reasons for the fiber structures at both ends being broken.

In addition, the specific surface areas of pure GaOOH and Ba-doped GaOOH were measured by using BET method. The BET results showed that the specific surface areas of pure GaOOH, 4 wt% Ba-doped GaOOH, 8 wt% Ba-doped GaOOH and 16 wt% Ba-doped GaOOH were 6.3047 $m^2 g^{-1}$, 21.5854 $m^2 g^{-1}$, 18.7497 $m^2 g^{-1}$ and 18.1918 $m^2 g^{-1}$, respectively. It was obvious that the Ba-doping significantly increased the specific surface area of GaOOH and the specific surface area of 4 wt% Ba-doped GaOOH was 3.42 times that of pure GaOOH. Compared with 4 wt% Ba-doped GaOOH, the specific surface area of 8 wt% Ba-doped GaOOH or 16 wt% Ba-doped GaOOH slightly decreased, which might result from the fracture of the fiber structures at both ends of GaOOH, as shown in Fig. 2.

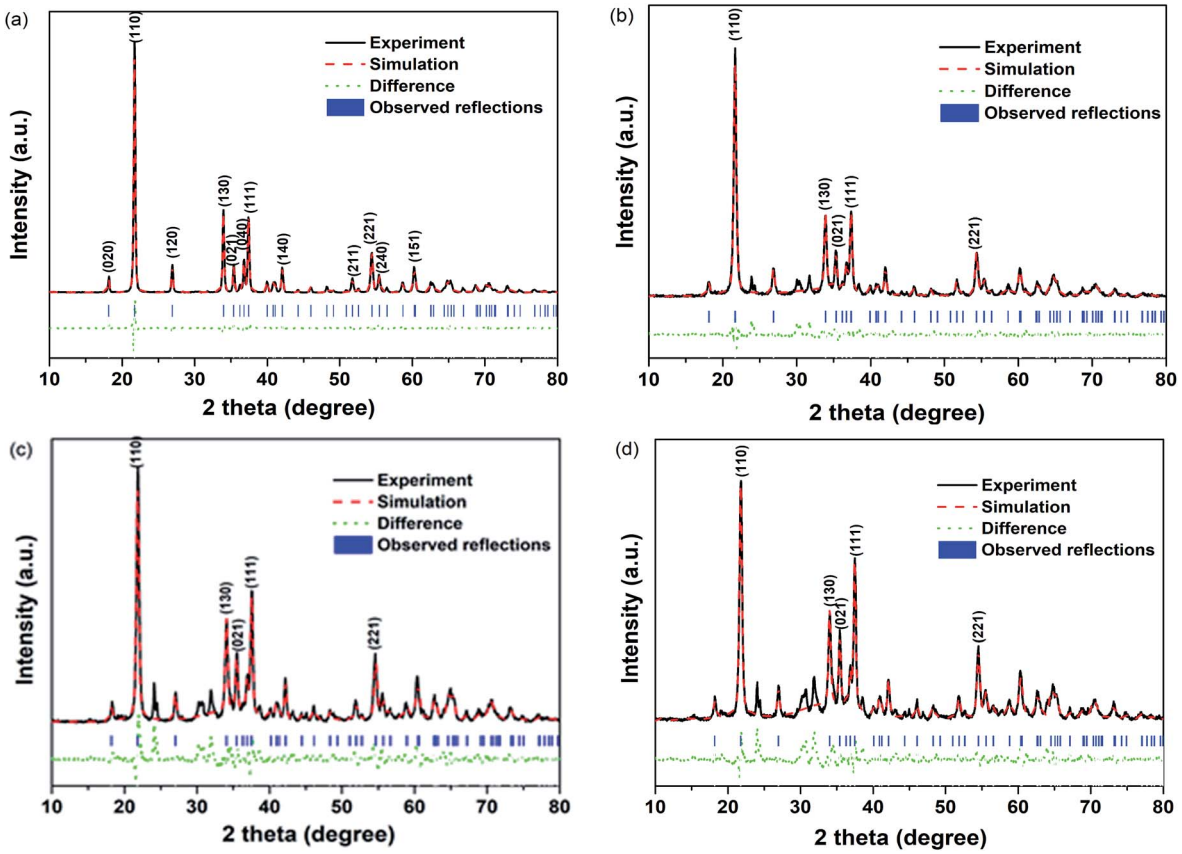

Fig. 1 XRD patterns and Pawley refinements of: (a) pure GaOOH; (b) 4 wt% Ba-doped GaOOH; (c) 8 wt% Ba-doped GaOOH; (d) 16 wt% Ba-doped GaOOH.

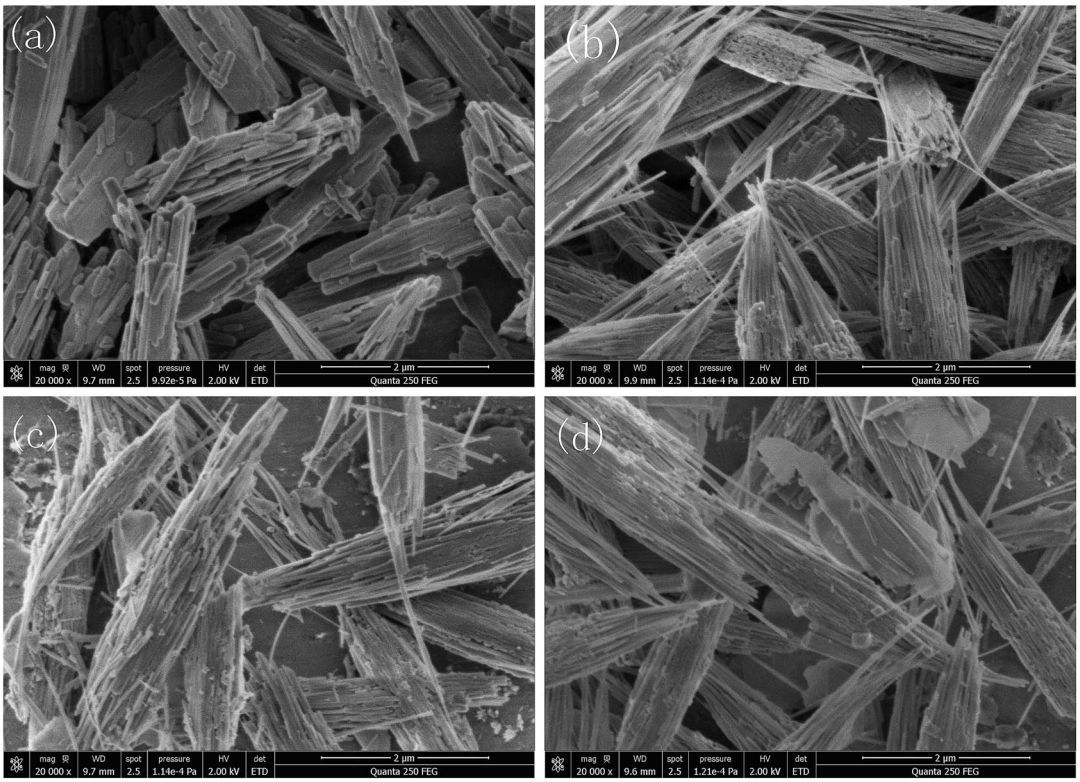

Fig. 2 SEM photographs of: (a) pure GaOOH; (b) 4 wt% Ba-doped GaOOH; (c) 8 wt% Ba-doped GaOOH; (d) 16 wt% Ba-doped GaOOH.

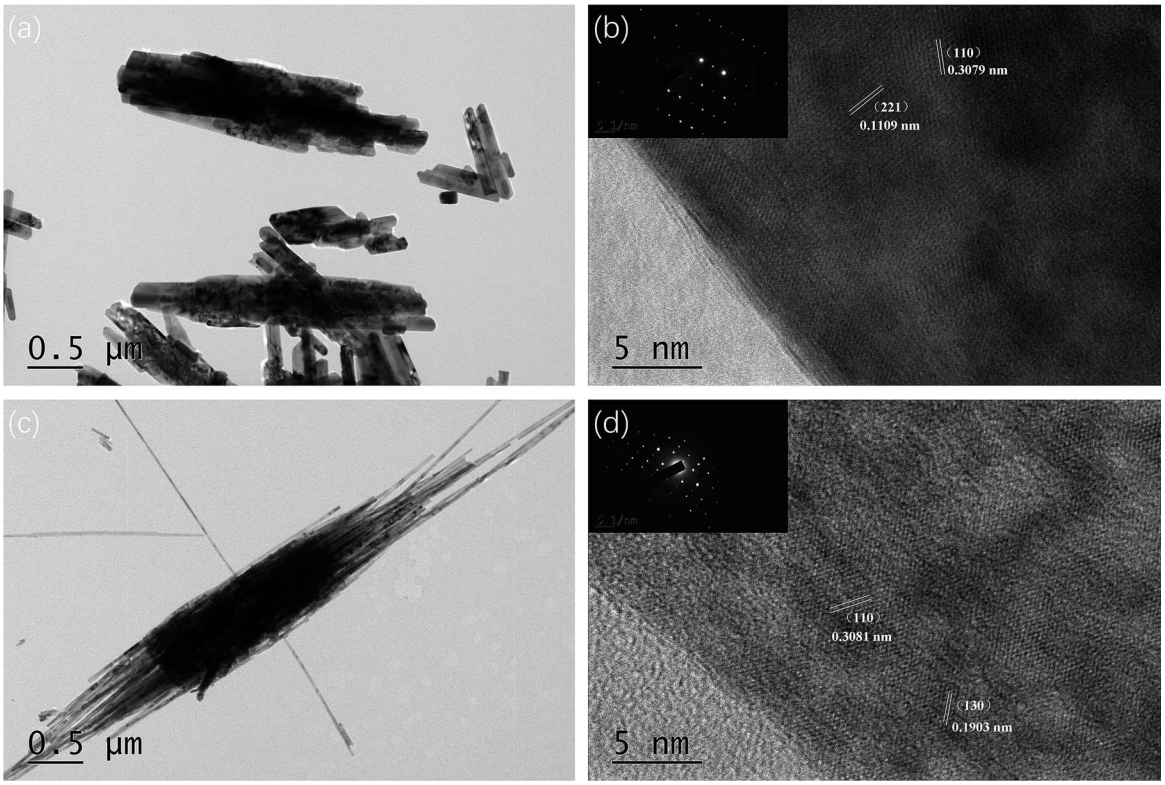

Fig. 3 The high resolution TEM pictures, the selected area electron diffraction (SAED) patterns and the HRTEM images with clear lattice fringe spacing for pure GaOOH (a and b) and 4 wt% Ba-doped GaOOH (c and d).

Fig. 3 shows the TEM information of pure GaOOH and 4 wt% Ba-doped GaOOH which included the high resolution TEM pictures, the SAED patterns and the HRTEM images with clear lattice fringe spacing. Regarding the morphology of the prepared samples, the TEM results were agree with the SEM pictures (Fig. 2). The fibrous structures at both ends of the 4 wt% Ba-doped GaOOH were observed clearly (Fig. 3(c)) and the diameter of the fiber rods was approximately 25 nm. Fig. 3(b and d) shows that the prepared pure GaOOH and 4 wt% Ba-doped GaOOH both had very good single crystal structure. Moreover, as shown in Fig. 3(b and d), (110) lattice plane of pure GaOOH and 4 wt% Ba-doped GaOOH was observed, which was also detected in the XRD patterns (Fig. 1).

XPS and FT-IR analysis. Fig. 4(a–c) shows the XPS spectra of Ba3d, Ga3d and O1s for 4 wt% Ba-doped GaOOH prepared by us. The binding energies of Ba3d, Ga3d and $Ga3d_{5/2}$ in Ba-doped GaOOH were 780.7, 20 and 21 eV, respectively. According to the XPS standard binding energy data, the valence of Ba, Ga and O element in 4 wt% Ba-doped GaOOH were confirmed to be +2, +3 and −2, indicating that the Ba element existed in the form of Ba^{2+} on the surface of GaOOH.

Fig. 4(d) shows the FT-IR spectra of pure GaOOH and GaOOH with different Ba-doping amount prepared by us. Compared to pure GaOOH, after Ba-doping, new peak appeared at and 1460 cm^{-1} and the peak intensity increased as the amount of Ba-doping increased, which should thus characterize the barium phase.[40] In addition, both pure GaOOH and Ba-doped GaOOH had broad peaks at 2900 cm^{-1} and sharp peaks at 1018 cm^{-1} and 948 cm^{-1}. Among them, the peak at 2900 cm^{-1} was attributed to the vibration of O–H in GaOOH,[29] and the peaks at 948 cm^{-1} and 1018 cm^{-1} were attributed to the constitutional Ga–OH bending mode and its overtones, respectively.[29,41] The relative strength and position of the two bands (948 cm^{-1} and 1018 cm^{-1}) were related to the shape of the GaOOH.[42] Pure GaOOH also showed peaks at 640 cm, while the position of the peak shifted slightly to the lower wavenumber after Ba-doping, as shown in Fig. 4(d), because Ba-doping changed the appearance of GaOOH (Fig. 2). The phenomenon that lattice vibration band was affected by the appearance of the sample was also observed on FeOOH.[43,44]

UV-Vis DRS analysis. Fig. 5 shows the UV-visible diffuse reflectance spectra of pure GaOOH and GaOOH with different Ba-doping amount prepared by us. All the samples prepared by us were white with the naked eyes, which meant that samples had no photoresponse in the visible range.[45] The Kubelka–Munk transformation method was used in our experiment to calculate absorbance. The optical absorption near the band edge of the crystalline semiconductors meets the formula:[46,47] $\alpha h\nu = A(h\nu - E_g)^n$, where α, ν, E_g, and A are absorption coefficient, light frequency, band gap, and proportional constant,

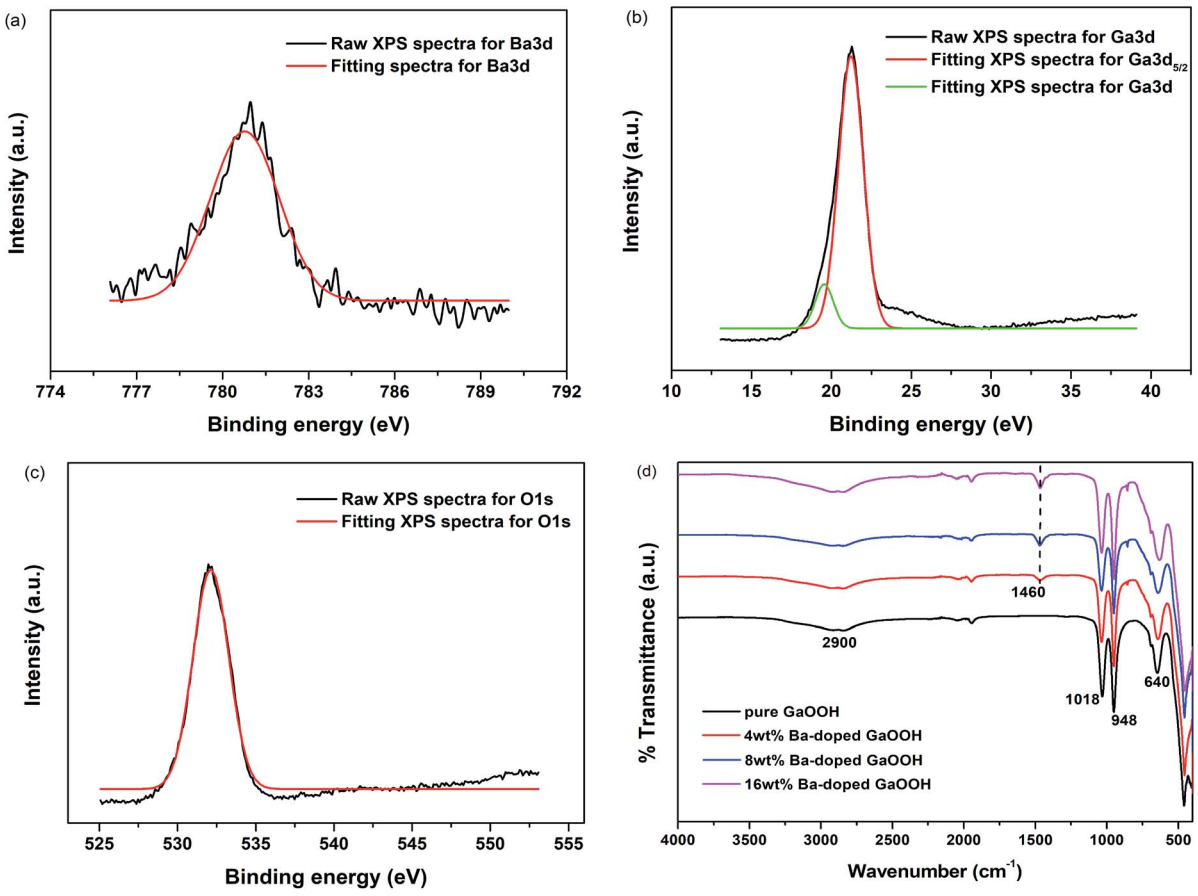

Fig. 4 XPS spectra of 4 wt% Ba-doped GaOOH ((a) Ba3d; (b) Ga3d; (c) O1s) and (d) FT-IR spectra of pure GaOOH and GaOOH with different Ba-doping amount.

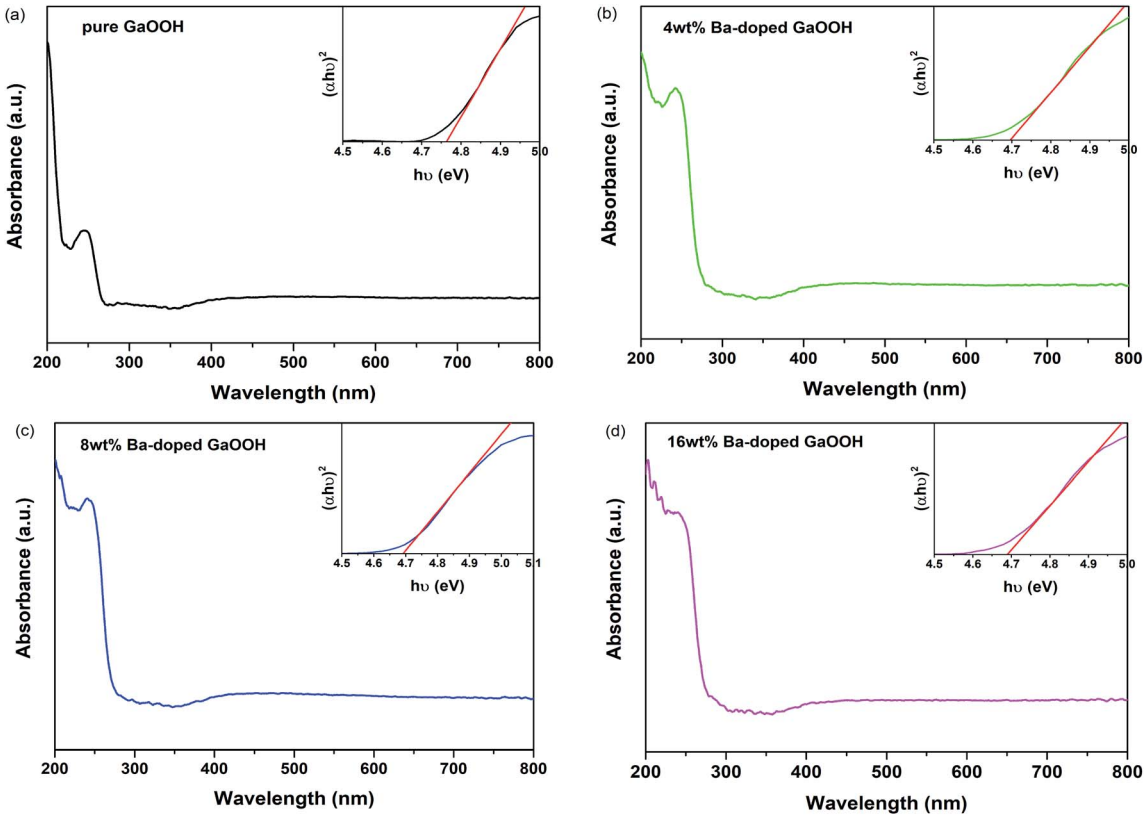

Fig. 5 UV-vis DRS spectra and band gaps of pure GaOOH and GaOOH with different Ba-doping amount.

respectively. According to the above formula, we obtained the values of band gap for pure GaOOH, 4 wt% Ba-doped GaOOH, 8 wt% Ba-doped GaOOH and 16 wt% Ba-doped GaOOH were 4.76 eV, 4.70 eV, 4.69 eV and 4.68 eV, respectively. Apparently, Ba-doping caused the absorption edge to move to long wavelength and the reason might be that the sp–d spin-exchanged between band electrons and the localized d electrons of the Ba ion.[28] Moreover, the calculated values of n were all 0.5 for pure GaOOH and Ba-doped GaOOH, which meant that the optical transition of prepared pure GaOOH and Ba-doped GaOOH all belonged to the type of direct transition.[48]

Band structure and PL analysis. Fig. 6(a and b) shows UPS spectra of pure GaOOH and 4 wt% Ba-doped GaOOH. According to the UPS results, the values of valence band of pure GaOOH and 4 wt% Ba-doped GaOOH were calculated to be 3.90 eV and 4.41 eV. Combined with the band gaps, the values of conduction band of pure GaOOH and 4 wt% Ba-doped GaOOH were obtained to be −0.86 eV and −0.29 eV. The band structures of pure GaOOH and 4 wt% Ba-doped GaOOH were shown in Fig. 6(c).

Fig. 6(d) shows the PL spectra of pure GaOOH and GaOOH with different Ba-doping amount prepared by us. As shown in Fig. 6(d), all samples showed a single emission peak at 315 nm. The PL emissions of samples might result from the recombination of the defect-related excitations through an excitation – excitation collision process.[49] After the samples were excited, electron–hole pairs were generated, wherein the holes were on the valence band or the defect-related position, and the electrons were on the conduction band or the defect-related position, and the two emitted photons during the recombination process, thereby the luminescence spectrums were generated as shown in Fig. 6(d). At an excitation wavelength of 280 nm, electron–hole pair generation was only attributed to defect-conduction band because the excitation energy of 280 nm light (4.43 eV) was lower than the band gaps of all samples prepared by us.[50] Thus, it was concluded that Ba-doping caused defects on GaOOH surface. As shown in Fig. 6(d), Ba-doping caused the decrease of emission peak intensity. When the amount of Ba-doping was 4 wt%, the intensity of emission peak was lowest, meaning that the recombination rate of electrons and holes was lowest, which provided a great possibility for the application of GaOOH in the field of photodegradation pollutants and hydrogen production.

Photocatalytic performance. As shown in Fig. 7(a), the absorbance of enrofloxacin at different concentrations (2 mg L^{-1}, 4 mg L^{-1}, 6 mg L^{-1}, 8 mg L^{-1}, 10 mg L^{-1} and 12 mg L^{-1}) in the range of 200–400 nm was tested by UV-visible spectrophotometer (UV-2550, Shimadzu Corporation, Kyoto, Japan). According to Fig. 7(a), the maximum absorption wavelength of enrofloxacin was determined to be 276 nm. The relationship between the concentration of enrofloxacin and the absorbance at 276 nm was shown in the Fig. 7(b). Using the unary linear regression method, we obtained the equation: $Y = 0.10632X + 0.01381$, where Y was the absorbance of enrofloxacin at 276 nm and X was the concentration of enrofloxacin. Correlation coefficient R^2 was 0.999, which meant linear regression result was good.

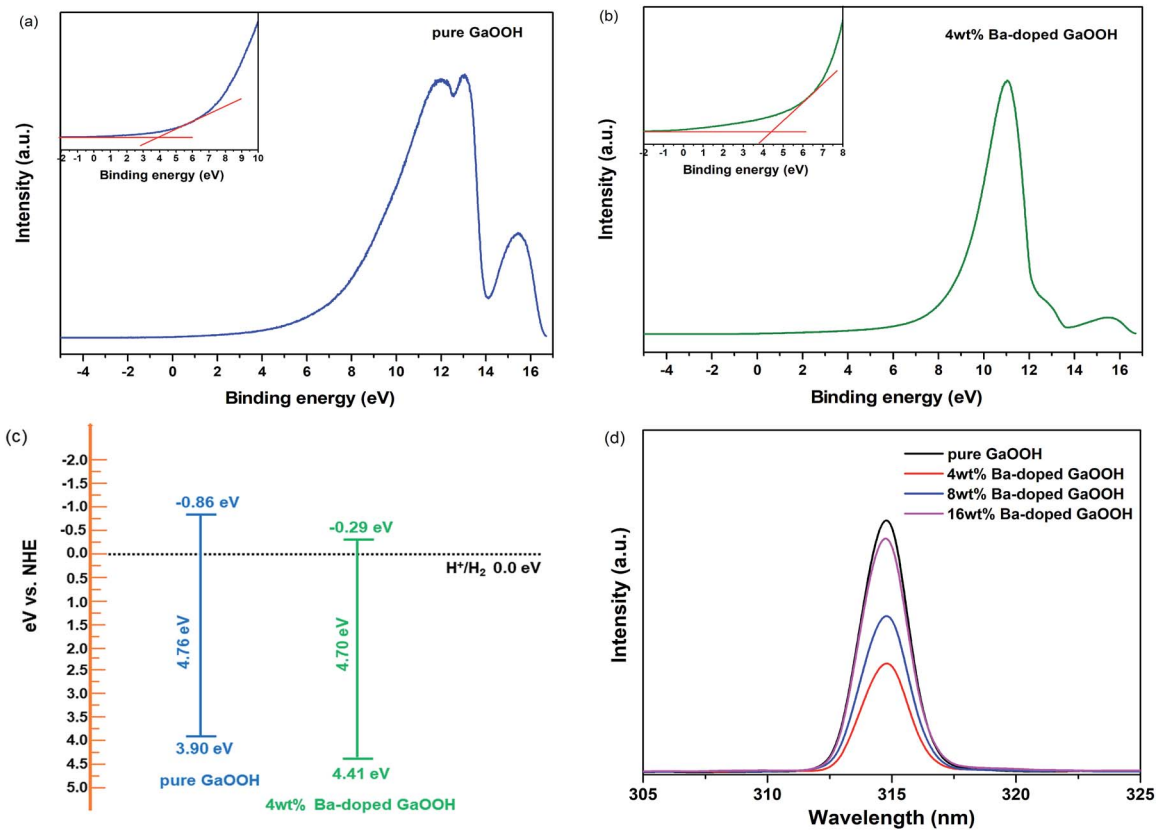

Fig. 6 (a and b) UPS spectra of pure GaOOH and 4 wt% Ba-doped GaOOH; (c) band structures of pure GaOOH and 4 wt% Ba-doped GaOOH; (d) PL spectra of pure GaOOH and GaOOH with different Ba-doping amount.

Fig. 8(a) shows the photocatalytic removal efficiency of enrofloxacin under UV light for 60 min with pure GaOOH and 4 wt%, 8 wt% and 16 wt% Ba-doped GaOOH as a photocatalyst, respectively. The results showed that the photocatalytic performance of GaOOH was significantly enhanced after Ba-doping. The removal rate of enrofloxacin by Ba-doped GaOOH was more than 20% higher than that of pure GaOOH. One of the reasons for the enhancement of the photocatalytic performance of Ba-doped GaOOH was the increase in specific surface area after Ba doping, according to the BET results.

Fig. 8(b) shows the photocatalytic removal efficiency of enrofloxacin at different initial pH using 4 wt% Ba-doped GaOOH as a photocatalyst. The results showed that the optimal initial pH for photocatalytic degradation of enrofloxacin by 4 wt% Ba-doped GaOOH was 7. In addition, when the initial pH was 5, 7, 9, and 11, the photocatalytic degradation efficiency of 4 wt% Ba-doped GaOOH on enrofloxacin did not change significantly, indicating that 4 wt% Ba-doped GaOOH photocatalyst had strong acid–base adaptability.

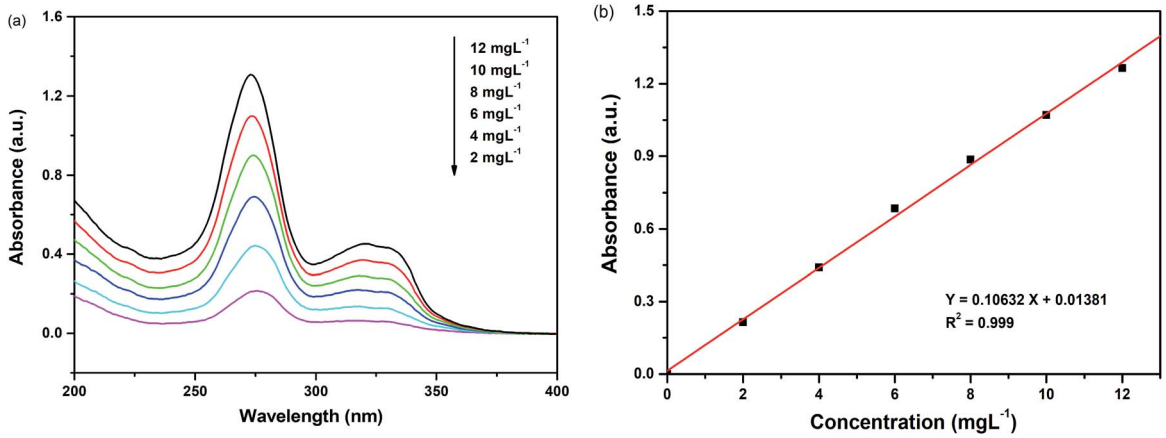

Fig. 7 (a) UV-Vis absorption spectra of different concentrations of enrofloxacin; (b) absorbency standard curve of enrofloxacin.

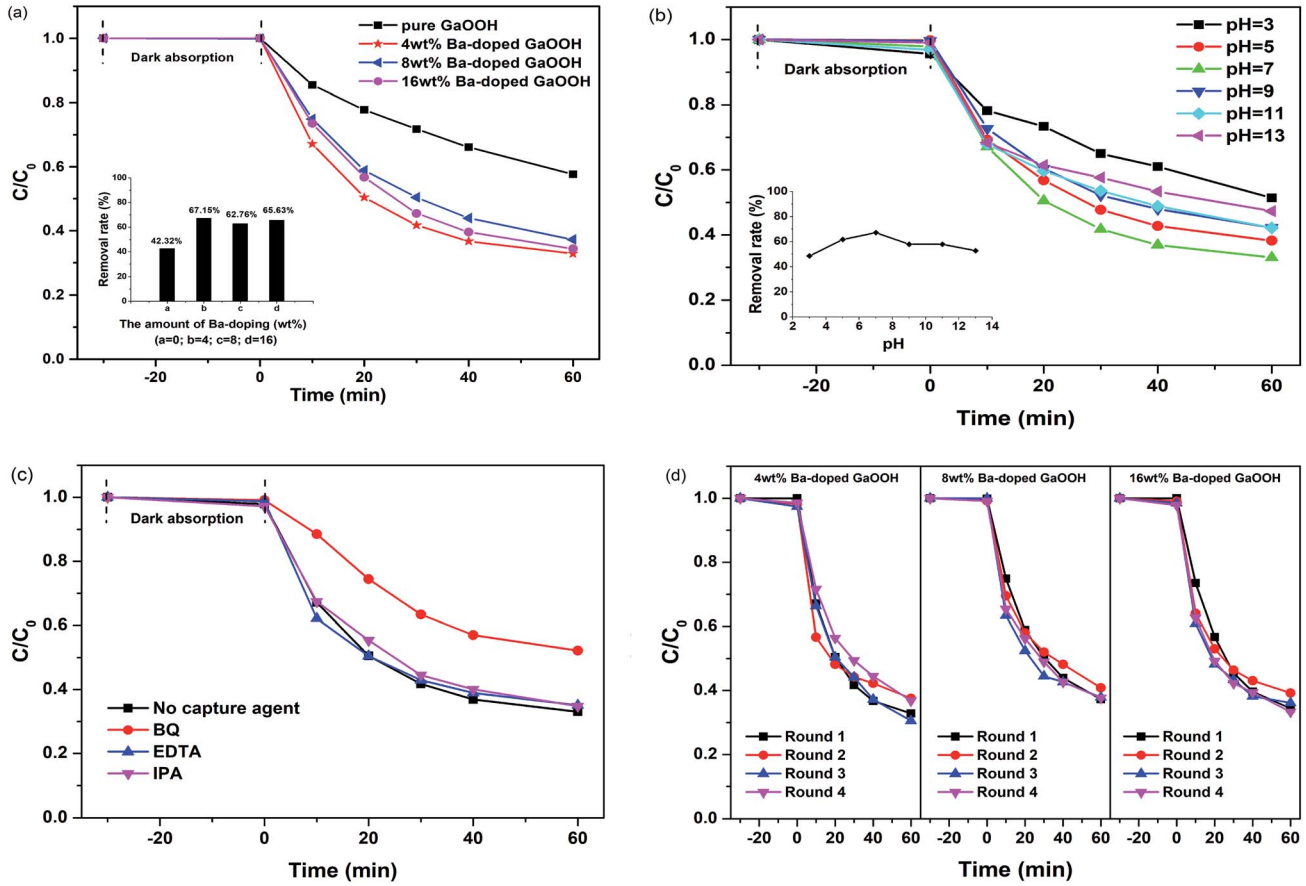

Fig. 8 (a) Removal of enrofloxacin by different photocatalysts with initial pH value of 7; (b) removal of enrofloxacin at different initial pH using 4 wt% Ba-doped GaOOH as a photocatalyst; (c) removal of enrofloxacin with the addition of different capture agents using 4 wt% Ba-doped GaOOH as a photocatalyst; (d) cyclic photocatalytic degradation of enrofloxacin using 4 wt%, 8 wt% and 16 wt% Ba-doped GaOOH as a photocatalyst, respectively.

Fig. 8(c) shows the photocatalytic removal efficiency of enrofloxacin with the addition of different capture agents using 4 wt% Ba-doped GaOOH as a photocatalyst. In this experiment, BQ (benzoquinone), EDTA (ethylenediaminetetraacetic acid) and IPA (isopropanol) acted as a capture agent for $\cdot O_2^-$, h^+ and $\cdot OH$, respectively. The addition amount of BQ, EDTA or IPA was set to be 1 mL and the concentration of BQ, EDTA or IPA was set to be 0.15 mmol L^{-1}. From Fig. 8(c), it was clearly that the addition of EDTA and IPA almost did not affect the photocatalytic degradation of enrofloxacin by 4 wt% Ba-doped GaOOH, but the addition of BQ significantly inhibited the photocatalytic degradation of enrofloxacin. Thus, it was

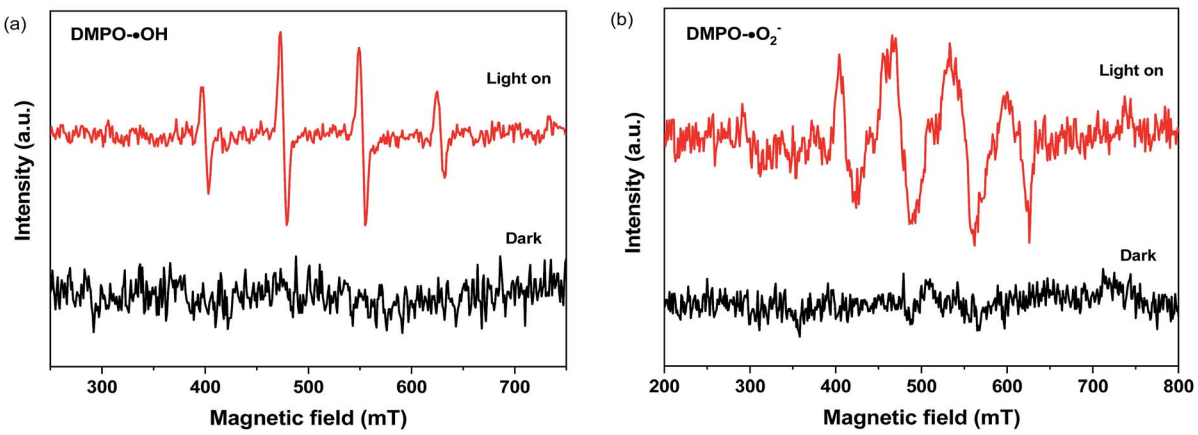

Fig. 9 DMPO spin-trapping EPR spectra of 4 wt% Ba-doped GaOOH in aqueous dispersion for DMPO–$\cdot OH$ (a) and in methanol dispersion for DMPO–$\cdot O_2^-$ (b).

concluded that in the process of photocatalytic degrading enrofloxacin, above active species could be ranked to increase photodegradation rate: $h^+ < \cdot OH < \cdot O_2^-$. In addition, the possible active radicals in the process of photocatalytic degrading enrofloxacin were measured by EPR characterization. Here, the 5,5-dimethyl-1-pyrroline *N*-oxide (DMPO) was used to spin traps the active radicals in the system for detection. As shown in Fig. 9, no EPR signals relevant to DMPO adducts were observed for 4 wt% Ba-doped GaOOH, when it was in darkness. However, after illumination, signals were observed in Fig. 9(a) and (b), corresponding with the DMPO/$\cdot$OH adduct and DMPO/$\cdot O_2^-$ adduct, respectively.

Fig. 8(d) shows the cyclic photocatalytic degradation of enrofloxacin using 4 wt%, 8 wt% and 16 wt% Ba-doped GaOOH as a photocatalyst, respectively. The results showed that in each of the four rounds of photocatalytic degradation experiments, the removal rates of enrofloxacin were basically the same, indicating that 4 wt%, 8 wt% and 16 wt% Ba-doped GaOOH had excellent stability and could be used repeatedly, which was beneficial to reduce the cost of catalyst in practical applications.

Conclusions

Ba-doped GaOOH prepared by solvothermal method was reported for the first time in this paper. According to XRD results, pure GaOOH and Ba-doped GaOOH were successfully prepared with the orthorhombic crystal system by space group *Pbnm* and the lattice parameters of GaOOH were $a = 4.509526$ Å, $b = 9.771034$ Å and $c = 2.969284$ Å. The morphology of GaOOH transformed from wood-like to rice husk-like structure after Ba-doping, which had many fibrous independent structures at both ends. It was obvious in BET results that the Ba-doping significantly increased the specific surface area of GaOOH and the specific surface area of 4 wt% Ba-doped GaOOH was 3.42 times that of pure GaOOH. UV-Vis DRS results revealed that Ba-doping decreased the band gap of GaOOH. In FT-IR results, the vibration peak caused by Ba doping was observed, indicating the successful doping of Ba. Moreover, Ba-doping caused defects on GaOOH surface, which decreased the combination rate of electrons and holes and enhanced the photocatalytic performance of GaOOH. The removal rates of enrofloxacin were 67.15%, 62.76%, 65.63% with 4 wt%, 8 wt% and 16 wt% Ba-doped GaOOH as a photocatalyst, respectively, higher than that of pure GaOOH (42.32%). Finally, it was found that Ba-doped GaOOH had good acid–base adaptability and good recyclability, which helps to reduce the cost in practical applications and greatly improves the practical application potential of GaOOH.

Conflicts of interest

There are no conflicts to declare.

Acknowledgements

This work was supported by the National Natural Science Foundation of China (No. 20877040). This work was supported by a grant from the Technological Supporting Foundation of Jiangsu Province (No. BE2009144). This work was supported by a grant from the Natural Science Foundation of Jiangsu Province (No. BK2007717, BK2006130). This work was supported by a grant from China-Israel Joint Research Program in Water Technology and Renewable Energy (No. 5).

References

1 M. Sun, D. Li, W. Zhang, X. Fu, Y. Shao, W. Li, G. Xiao and Y. He, *Nanotechnology*, 2010, **21**, 355601.
2 H. S. Qian, P. Gunawan, Y. X. Zhang, G. F. Lin, J. W. Zheng and R. Xu, *Cryst. Growth Des.*, 2008, **8**, 1282.
3 C. C. Huang and C. S. Yeh, *New J. Chem.*, 2010, **34**, 103.
4 S. Yan, L. Wan, Z. Li, Y. Zhou and Z. Zhou, *Chem. Commun.*, 2010, **46**, 6388.
5 L. H. Shi, J. Zhang, S. Wu, Y. A. Li, L. N. Jiang and Q. L. Cui, *J. Am. Ceram. Soc.*, 2014, **97**, 2607–2614.
6 H. K. Lee, M. S. Kim and J. S. Yu, *IEEE Photonics Technol. Lett.*, 2012, **24**, 285–287.
7 B. Zhan, Q. Cui, W. Liu and J. Zhang, *Chin. J. Chem.*, 2009, **27**, 2175–2177.
8 S. Yan, J. Wang, H. Gao and N. Y. Wang, *Adv. Funct. Mater.*, 2013, **23**, 758–763.
9 W. S. Jung and B. K. Min, *Mater. Lett.*, 2004, **58**, 3058–3062.
10 S. Ge, L. Zhang, H. M. Jia and Z. Zheng, *J. Mater. Res.*, 2009, **24**, 2268–2275.
11 A. C. Tas, P. J. Majewski and F. J. Aldinger, *J. Am. Ceram. Soc.*, 2002, **85**, 1421.
12 M. Muruganandham, R. Suri, M. S. M. Abdel Wahed, M. Sillanpá, B. Ahmmad, G. J. Lee and J. J. Wu, *Mater. Lett.*, 2013, **111**, 137.
13 A. C. Tas, P. J. Majewski and F. Aldinger, *J. Am. Chem. Soc.*, 2002, **85**, 1421–1429.
14 I. Lee, J. Kwak, S. Haam and S. Lee, *J. Cryst. Growth*, 2010, **312**, 2107–2112.
15 S. G. Chen, S. M. Luo, Y. Zhou, Y. Chen, Y. Q. Liu and C. G. Long, *Mater. Lett.*, 2008, **62**, 4566–4569.
16 D. Li, X. C. Duan, Q. Qin, H. M. Fan and W. J. Zheng, *J. Mater. Chem. A*, 2013, **1**, 12417.
17 F. Shiba, M. Yuasab and Y. Okawa, *CrystEngComm*, 2018, **20**, 4910.
18 B. Lertanantawong, J. D. Riches and A. P. O'Mullane, *Langmuir*, 2018, **34**, 7604–7611.
19 M. Muruganandham, R. Amutha, M. S. M. Abdel Wahed, B. Ahmmad, T. Ohkubo, R. P. S. Suri, J. J. Wu and M. Sillanpää, *J. Phys. Chem. C*, 2012, **116**, 44–53.
20 Y. H. Hsu, A. T. Nguyen, Y. H. Chiu, J. M. Li and Y. J. Hsu, *Appl. Catal., B*, 2016, **185**, 133–140.
21 P. Bouras, E. Stathatos and P. Lianos, *Appl. Catal., B*, 2007, **73**, 51–59.
22 X. C. Meng and Z. S. Zhang, *Appl. Surf. Sci.*, 2017, **392**, 169–180.
23 F. Bensouici, M. Bououdina, A. A. Dakhel, R. Tala-Ighil, M. Tounane, A. Iratni, T. Souier, S. Liu and W. Cai, *Appl. Surf. Sci.*, 2017, **395**, 110–116.

24 A. Tabib, W. Bouslama, B. Sieber, A. Addad, H. Elhouichet, M. Férid and R. Boukherrou, *Appl. Surf. Sci.*, 2017, **396**, 1528–1538.
25 S. S. Xue, H. B. He, Q. Z. Fan, C. L. Yu, K. Yang, W. Y. Huang, Y. Zhou and Y. Xie, *J. Environ. Sci.*, 2017, **60**, 70–77.
26 C. Li, Z. Yan and Z. Yuan, *Funct. Mater. Lett.*, 2018, **11**, 1750082.
27 A. Firdous, M. A. Baba, D. Singh and A. H. Bhat, *Appl. Nanosci.*, 2015, **5**, 201–206.
28 G. Srinet, R. Kumar and V. Sajal, *Mater. Lett.*, 2014, **126**, 274–277.
29 G. G. Li, C. Peng, C. X. Li, P. P. Yang, Z. Y. Hou, Y. Fan, Z. Y. Cheng and J. Lin, *Inorg. Chem.*, 2010, **49**, 1449–1457.
30 S. Basu, B. S. Naidu, M. Pandey, V. Sudarsan, S. N. Jha, D. Bhattacharyya, R. K. Vatsa and R. J. Kshirsagar, *Chem. Phys. Lett.*, 2012, **528**, 21–25.
31 B. S. Naidu, M. Pandey, J. Nuwad, V. Sudarsan, R. K. Vatsa, R. J. Kshirsagar and C. G. S. Pillai, *Inorg. Chem.*, 2011, **50**, 4463–4472.
32 L. Binet, D. Gourier and C. Minot, *J. Solid State Chem.*, 1994, **113**, 420–433.
33 N. Ueda, H. Hosono, R. Waseda and H. Kawazoe, *Phys. Lett.*, 1997, **71**, 933–935.
34 T. Miyata, T. Nakatani and T. Minami, *Thin Solid Films*, 2000, **373**, 145–149.
35 E. G. Villora, T. Atou, T. Sekiguchi and T. Sugawara, *Solid State Commun.*, 2001, **120**, 455–458.
36 M. Ogita, K. Higo, Y. Nakanishi and Y. Hatanaka, *Appl. Surf. Sci.*, 2001, **721**, 175–176.
37 J. F. Luan and P. Q. Huang, *Materials*, 2018, **11**, 491.
38 A. C. Taş, P. J. Majewski and F. Aldinger, *J. Am. Ceram. Soc.*, 2002, **85**, 1414–1420.
39 R. Elilarassi and G. Chandrasekaran, *Mater. Chem. Phys.*, 2010, **123**, 450–455.
40 S. P. D. Valle, O. Marie and H. P. Nguyen, *Appl. Catal., B*, 2018, **223**, 116–124.
41 X. H. Liu, G. Z. Qiu, Y. Zhao, N. Zhang and R. Yi, *J. Alloys Compd.*, 2007, **439**, 275–278.
42 S. Krehula, M. Ristić, S. Kubuki, Y. Iida, M. Fabián and S. Musić, *J. Alloys Compd.*, 2015, **620**, 217–227.
43 S. Krehula, S. Popović and S. Musić, *Mater. Lett.*, 2002, **54**, 108–113.
44 S. Krehula and S. Musić, *J. Cryst. Growth*, 2008, **310**, 513–520.
45 S. M. Hong, C. K. Rhee and Y. Sohn, *J. Alloys Compd.*, 2019, **774**, 11–17.
46 J. Tauc, R. Grigorov and A. Vancu, *Phys. Status Solidi*, 1966, **15**, 627–637.
47 M. A. Butler, *J. Appl. Phys.*, 1977, **48**, 1914–1920.
48 J. F. Luan, Y. Shen, S. Wang and N. B. Guo, *Polymers*, 2017, **9**, 69.
49 S. Wu, J. Zhang, L. Shi, S. Tang, Y. Li, L. Jiang and Q. Cui, *RSC Adv.*, 2014, **4**, 8209–8215.
50 X. Xu, K. Bi, K. Huang, C. Liang, S. Lin, W. J. Wang, T. Z. Yang, J. Liu, D. Y. Fan, H. J. Yang, Y. G. Wang and M. Lei, *J. Alloys Compd.*, 2015, **644**, 485–490.